Progress In Electromagnetics Research B, Vol. 46, 317–336, 2013

ATTACHMENT MODES IN THE METHOD OF MOMENTS IN TIME-DOMAIN

Elson Agastra, Giuseppe Pelosi, and Stefano Selleri*

Department of Electronic and Telecommunications, University of Florence, Via di Santa Marta, 3, Florence I-50123, Italy

Abstract—Efficient and accurate modeling of electromagnetic structures is valuable in antenna analysis and design, and time domain solutions are at a premium over frequency domain in the case of ultra wide band signals or transients. Among the full wave electromagnetic methods in time domain the method of moments in time domain (MoM-TD) is very interesting. Such a method can be implemented, as for frequency domain, either resorting to a thin wire approximation or to a surface patch model. Depending on the structure to be analyzed one or the other is most convenient. For heterogeneous structures both implementations might be needed, and the problem of the attachment between a perfectly conducting thin wire and a perfectly conducting surface is hence relevant. In this paper, attachment modes are introduced in MoM-TD. The solution is validated on a test case and against another numerical technique.

1. INTRODUCTION

When dealing with ultra wide band (UWB) signals and transients, a single time domain analysis is usually more efficient than having to perform several frequency domain analyses at the relevant frequencies in the spectrum of the UWB signal and then perform an inverse Fourier transform (IFT). Among the various time domain techniques, the method of moments in time domain (MoM-TD) is less investigated than others like, for example, finite difference in time domain (FD-TD) or finite elements in time domain (FE-TD); yet MoM-TD, being an integral equation method based on currents, share the same advantages of the frequency domain MoM over frequency based techniques exploiting differential equations and fields: the domain to be

Received 17 October 2012, Accepted 5 December 2012, Scheduled 7 December 2012

* Corresponding author: Stefano Selleri (stefano.selleri@unifi.it).

discretized are surfaces, thus 2D and not 3D, and radiation boundary conditions are implicit in the formulation [1, 2].

Field computation via MoM-TD is not a new concept; it was proposed in the 60s [3] but has not been applied to practical electromagnetic engineering problems until recent times. There are some papers on MoM-TD relative both to thin wire approximation (TWA) [2] and to surface patch model (SPM) [1, 4–6] developed either via implicit or explicit time schemes. In all these approaches the major issue appears to be that of late time stability, indeed the solutions have a strong tendency to exponentially diverge as the time marching scheme proceeds [7, 8].

The authors have presented recently an implementation of both thin wire and surface patch MoM-TD in an unified approach [9, 10], also presenting new time basis function aimed at higher stability and insights on how to enhance stability via explicit filtering [10]. In such implementation the scattering body can be either a wire grid model (WGM) or a SPM and unconnected bodies modeled either via SPM or WGM can be present in the same simulation.

To analyze a scatterer whose model contains both a WGM and a SPM part an appropriate model for the junction, or attachment, between wires and surface patches is necessary. Such an attachment is commonly treated in method of moments in frequency domain [11–15] but is less investigated in time domain.

This paper is mainly devoted to present the theory and the implementation of a space basis function for the attachment in time domain. Secondarily, in this paper the computation of transient scattered fields is also performed, whereas previous papers only dealt with currents [9, 10].

This paper is organized as follows: Section 2 will briefly summarize the MoM-TD method, with an unified notation valid for wires, patches and attachments. Section 3 will describe the space base functions and test functions peculiar to the attachment, the details relevant to wires and patches being given in [9, 10]. Section 4 will describe the transient radiated field theory and implementation. Section 5 will present numerical results, and finally Section 6 will draw some conclusions.

2. THEORY

A generic scattering body S may contain a planar part S_T to be subdivided into a mesh-grid of planar patches and a wire part S_W to be subdivided into a mesh-grid of piece-wise rectilinear segments of radius a as shown in Figure 1. For each non-boundary edge in

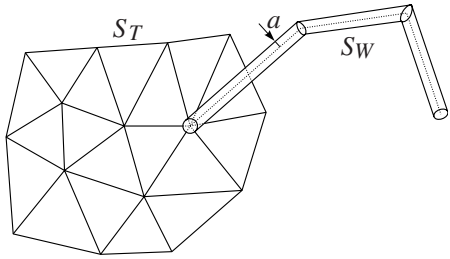

Figure 1. Scattering body with planar and wire part connected.

S_T a Rao-Wilton-Glisson (RWG) spatial basis is defined along the two triangular patches sharing it [10, 16] and for each non boundary node in S_W a wire basis function is defined on the two wire segments sharing it [1, 9]. The attachment comprises one or more triangular patches, sharing a vertex node, and one segment connected to that same node.

By deriving the tangential electric field continuity condition with respect to time and considering the continuity equation for charge and current, a variant of the standard EFIE equation can be obtained [1, 5]

$$\left[\frac{\partial^2 \mathbf{a}\left(\mathbf{r},t\right)}{\partial t^2}+\nabla\psi\left(\mathbf{r},t\right)\right]_{\tan}=\left[\frac{\partial \mathbf{e}^i\left(\mathbf{r},t\right)}{\partial t}\right]_{\tan} \tag{1}$$

being

$$\mathbf{a}\left(\mathbf{r},t\right)=\frac{\mu}{4\pi}\int_S \frac{\mathbf{j}\left(\mathbf{r}',\tau\right)}{|\mathbf{r}-\mathbf{r}'|}d\mathbf{r}' \tag{2}$$

the vector potential;

$$\psi\left(\mathbf{r},t\right)=-\frac{1}{4\pi\varepsilon}\int_S \frac{\nabla'\cdot\mathbf{j}\left(\mathbf{r}',\tau\right)}{|\mathbf{r}-\mathbf{r}'|}d\mathbf{r}' \tag{3}$$

the scalar potential, and

$$\tau=t-\frac{|\mathbf{r}-\mathbf{r}'|}{c} \tag{4}$$

the delay between source point $\mathbf{r}'$ on $S=S_T\cup S_W$, and the generic observation point $\mathbf{r}$. Finally $\mathbf{e}^i\left(\mathbf{r},t\right)$ is the impressed incident electric field. The wire current distributions $\mathbf{j}\left(\mathbf{r}',t\right)$ are assumed concentrated on the wire axis and directed only along it, while planar current distributions are constrained on S_T. The unknown current distribution is then discretized exploiting two set of bases: a set of time bases $T_h\left(t\right)$ and a set of space bases $\mathbf{f}_k\left(\mathbf{r}\right)$

$$\mathbf{j}(\mathbf{r},t)=\sum_{k=0}^{N_T-1}\sum_{h=0}^{M-1}J_k^h T_h\left(t\right)\mathbf{f}_k^T\left(\mathbf{r}\right)$$

$$+\sum_{k=0}^{N_W-1}\sum_{h=0}^{M-1} J_k^h T_h(t)\,\mathbf{f}_k^W(\mathbf{r}) + \sum_{k=0}^{N_A-1}\sum_{h=0}^{M-1} J_k^h T_h(t)\,\mathbf{f}_k^A(\mathbf{r}) \quad (5)$$

where $\mathbf{f}_k^T$, $\mathbf{f}_k^W$ and $\mathbf{f}_k^A$ are the space basis functions defined on inner edges (triangular patches), inner nodes (wires) and attachments, respectively, and N_T, N_W and N_A are their respective total number and M the number of time steps on which the simulation is performed. J_k^h are the unknown current distribution coefficients to be determined.

While space basis functions are the same than in frequency domain [5], time basis $T_h(t)$ might need to be detailed. Given the discretization Δt of the time axis, time basis are defined as a single function $T(t)$ translated along the time axis, according to:

$$T_h(t) = T(t - h\Delta t) \quad (6)$$

The time basis $T_h(t)$ is usually selected as a C^0 (continuous) or more regular (C^1, continuous and differentiable) function whose value is 1 for $t = 0$ and zero for $t = n\Delta t$ for non-zero integer values of n. The choice of these interpolation functions is far from being trivial because it deeply affects both accuracy and stability, as analyzed in [9].

To complete the weighted residual scheme, a set of test functions, ${}_m\mathbf{w}(\mathbf{r})$, and a suitable inner product, $\langle\cdot,\cdot\rangle$, must be defined. It is then possible to *project* Equation (1) in the inner product definition space and evaluate the solution coefficients. Equation (1) becomes:

$$\left\langle \frac{\partial^2 \mathbf{a}(\mathbf{r},t)}{\partial t^2}, {}_m\mathbf{w} \right\rangle + \langle \nabla\psi(\mathbf{r},t), {}_m\mathbf{w}\rangle = \left\langle \frac{\partial \mathbf{e}^i(\mathbf{r},t)}{\partial t}, {}_m\mathbf{w} \right\rangle \quad (7)$$

where the inner product projection implicitly select the tangential component of (1). By discretizing the second time derivative of the unknown potential with backward differences one obtains:

$$\begin{aligned}&\langle \mathbf{a}^n(\mathbf{r}), {}_m\mathbf{w}\rangle - 2\left\langle \mathbf{a}^{n-1}(\mathbf{r}), {}_m\mathbf{w}\right\rangle + \left\langle \mathbf{a}^{n-2}(\mathbf{r}), {}_m\mathbf{w}\right\rangle \\ &+\Delta t^2 \langle \nabla\psi^n(\mathbf{r}), {}_m\mathbf{w}\rangle = \Delta t^2 \left\langle \dot{\mathbf{e}}^i(\mathbf{r},t), {}_m\mathbf{w}\right\rangle \end{aligned} \quad (8)$$

where superscript n indicates the n-th time sample of a given function (i.e., $\mathbf{a}^n(\mathbf{r}) = \mathbf{a}(\mathbf{r}, n\Delta t)$) and $\dot{\mathbf{e}}^i(\mathbf{r},t)$ is the time derivative of the impressed field.

The choice of a backward second order finite difference approximation has been preferred of a conventional central finite difference because, as it has been shown in [9] the use of backward instead of central finite difference schemes does not influence the accuracy, but has a very important positive impact on the numerical stability of the algorithm.

Note that subscripts and superscripts are placed at the right of the symbol when they refer to the basis, as in (5), and to the left when they refer to the test functions, as in (8).

The expressions of the scalar and vector potential at a given time step appearing in (8), can be immediately obtained by casting (5) into (2) and (3). With this consideration, and by rearranging (8) so that all terms at current time step n are in the left-side term and all the terms in $n-1$ and $n-2$ are on the right-side term, a marching-in-time scheme is obtained [9, 10].

3. SPATIAL BASES

In this work, without loss of generality, the attachment of a single wire to an arbitrary number of triangles, non necessarily co-planar, will be considered. For coherence with the definitions in [10] the superscript + conventionally indicates surface part of the domain while the superscript − indicates the wire part. Referring to the structure shown in Figure 2 the symbols used in this section are:

k: index of the generic attachment;

L_k: total number of triangles forming the surface part;

$\mathscr{T}_{ki}$: ith triangle of the kth attachment;

$\mathscr{W}_k$: wire attached at the common node;

$\boldsymbol{\rho}_{ki}^{+} = (\mathbf{r} - \mathbf{r}_k)$: local vector from the junction vertex to a generic point on $\mathscr{T}_{ki}$; no subscript i is present in $\mathbf{r}_k$ since it is the common vertex to all triangles belonging to the attachment;

$\boldsymbol{\rho}_{k}^{-} = \left(\mathbf{r}_k^{-} - \mathbf{r}\right)$: local vector in wire $\mathscr{W}_k$;

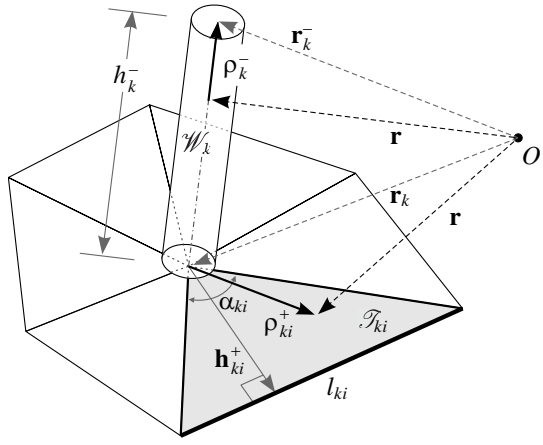

Figure 2. Attachment domain: triangles defining the surface domain and a segment defining its wire domain of a basis/test function. Triangles do not need to be co-planar.

h_{ki}^{+}: the height of triangle i, associated with the edge opposite to the junction vertex;
h_{k}^{-}: length of the wire $\mathscr{W}_k$;
l_{ki}: length of the edge opposite to the attachment node in triangle i;
α_{ki}: angle at the junction vertex for triangle i;
α_{k}^{t}: sum of the angles α_{ki};
K_{ki}: current spreading factor; $K_{ki} = \frac{\alpha_{ki}}{l_{ki}\sum_{i=1}^{L_k}\alpha_{ki}} = \frac{\alpha_{ki}}{l_{ki}\alpha_k^t}$.

The analytic form of the spatial basis chosen for the attachment modes introduced in [11–15] for the frequency domain MoM will be here applied to the time domain MoM:

$$\mathbf{f}_k(\mathbf{r}) = \begin{cases} K_{ki}\left[1 - \frac{\left(h_{ki}^{+}\right)^2}{\left(\boldsymbol{\rho}_{ki}^{+}\cdot\hat{\mathbf{h}}_{ki}^{+}\right)^2}\right]\frac{\boldsymbol{\rho}_{ki}^{+}}{h_{ki}^{+}} & \mathbf{r}\in\mathscr{T}_{ki} \\ \frac{\boldsymbol{\rho}_{k}^{-}}{h_{k}^{-}} & \mathbf{r}\in\mathscr{W}_k \\ 0 & \text{elsewhere} \end{cases} \tag{9}$$

In a weight residual framework, a suitable set of test functions ${}_m\mathbf{w}(\mathbf{r})$ must be also defined on the scattering body geometry. In a Galerkin approach, these can be chosen equal to the basis functions, and for the attachment modes, (9) can be used, being m the index of the attachment domain where the test function is defined.

The first three terms in (8), containing vector potential $\mathbf{a}(\mathbf{r})$ differ from each other only for the time step index n; while the right hand side term contains the electric field rather than the vector potential, but is formally identical to the others, hence just one need to be investigated:

$$\langle \mathbf{a}^n(\mathbf{r}),_m \mathbf{w}(\mathbf{r})\rangle = \int\limits_{{}_m^{\pm}\mathscr{D}} \mathbf{a}^n(\mathbf{r})\cdot_m \mathbf{w}(\mathbf{r})\; d\mathbf{r} \tag{10}$$

where ${}_m^{\pm}\mathscr{D}$ is a formal expression to indicate that the integration is carried out on the domain of the test ${}_m\mathbf{w}$ function, comprising two parts, conventionally indicated as ${}_m^{+}\mathscr{D}$ and ${}_m^{-}\mathscr{D}$. The actual domain for each model is given in Table 1 (see also Figure 3).

Expanding the test function domain ${}_m^{\pm}\mathscr{D}$ for the attachment, (10) can be recast in:

$$\langle \mathbf{a}^n(\mathbf{r}),_m \mathbf{w}(\mathbf{r})\rangle = \sum_{l=1}^{L_m}\left\{\mathbf{a}^n({}_{ml}^{+c}\mathbf{r})\cdot\iint\limits_{{}_{ml}\mathscr{T}} {}_m^{+}\mathbf{w}(\mathbf{r})\,dS\right\} + \mathbf{a}^n({}_m^{-c}\mathbf{r})$$

$$\cdot\int\limits_{{}_m\mathscr{W}} {}_m^{-}\mathbf{w}(\mathbf{r})\,dl = \sum_{l=1}^{L_m}\mathbf{a}^n({}_{ml}^{+c}\mathbf{r})\cdot\left[{}_{ml}^{+}\mathbf{W}\right] + \mathbf{a}^n({}_m^{-c}\mathbf{r})\cdot\left[{}_m^{-}\mathbf{W}\right] \tag{11}$$

Table 1. Generic to particular domain mappings.

	WGM	SPM	ATT
$\overset{+}{m}\mathscr{D}$	$\overset{+}{m}\mathscr{W}$	$\overset{+}{m}\mathscr{T}$	$\overset{+}{ml}\mathscr{T}$ with $l = 1, \ldots, L_m$
$\overset{-}{m}\mathscr{D}$	$\overset{-}{m}\mathscr{W}$	$\overset{-}{m}\mathscr{T}$	$\overset{-}{m}\mathscr{W}$

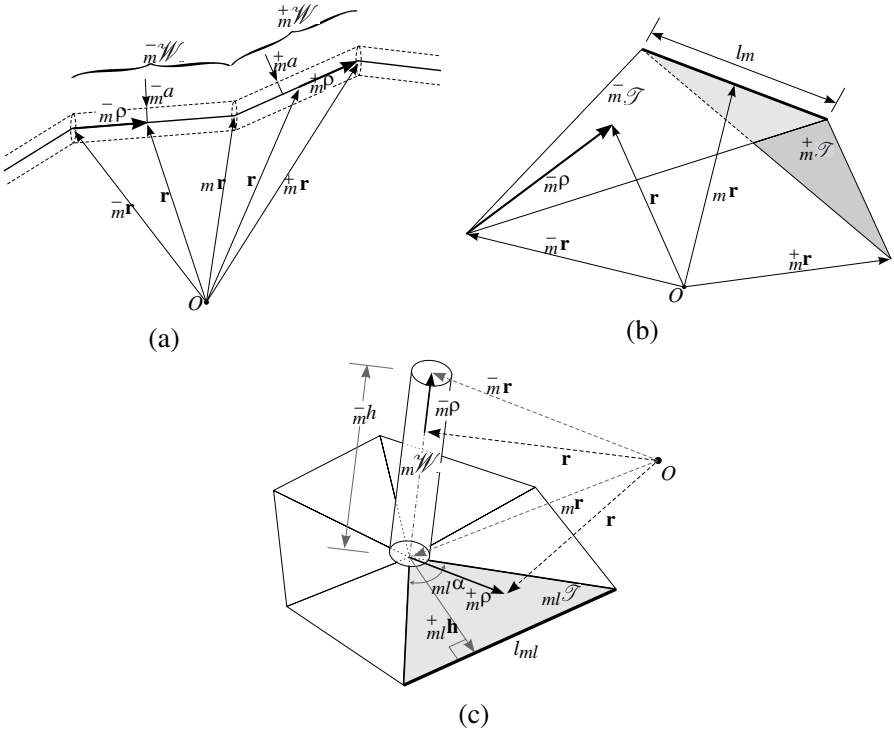

Figure 3. Test and base functions spatial domain. (a) Thin wire domain. (b) Surface patch domain. (c) Attachment domain.

where $\overset{+c}{ml}\mathbf{r}$ is the central point of $\overset{+}{ml}\mathscr{T}$, and $\overset{-c}{m}\mathbf{r}$ is the central point of $\overset{-}{m}\mathscr{W}$. In (11), the vector potential $\mathbf{a}^n(\mathbf{r})$ is considered uniform on each subdomain and hence can be extracted from the integral, leading to values $\left[\overset{\pm}{ml}\mathbf{W}\right]$, which can be computed only once for a given geometry. This approximation corresponds to a first-order Gaussian quadrature and it is acceptable if the maximum dimension of the sub-domains is much smaller than the minimum wavelength of the excitation signal.

With a similar procedure, the term relative to the scalar potential is approximated by applying the vector Green's identity and the properties of test functions:

$$\langle \nabla\psi^n(\mathbf{r}), {}_m\mathbf{w}\rangle = -\int_{{}^{\pm}_{m}\mathscr{D}} \psi^n(\mathbf{r})\,\nabla\cdot{}_m\mathbf{w}(\mathbf{r})\,d\mathbf{r}$$

$$= -\sum_{l=1}^{L_m}\left\{\psi^n({}^{+c}_{ml}\mathbf{r})\cdot\iint_{{}_{ml}\mathscr{T}}\nabla\cdot{}^{+}_{m}\mathbf{w}(\mathbf{r})\,dS\right\} - \psi^n({}^{-c}_{m}\mathbf{r})\cdot\int_{{}_{m}\mathscr{W}}\nabla\cdot{}^{-}_{m}\mathbf{w}(\mathbf{r})\,dl$$

$$= \sum_{l=1}^{L_m}\psi^n\left({}^{+c}_{ml}\mathbf{r}\right)\left[{}^{+}_{ml}M\right] + \psi^n\left({}^{-c}_{m}\mathbf{r}\right)\left[{}^{-}_{m}M\right] \tag{12}$$

the divergence of the test functions — which in a Galerkin approach are equal to the basis functions — can be analytically computed, and no singularity arise [12, 13, 17]:

$$\nabla\cdot{}_m\mathbf{w}(\mathbf{r}) = \frac{\partial}{\partial\rho}\left({}_m\mathbf{w}(\mathbf{r})\cdot\hat{\boldsymbol{\rho}}\right) = \begin{cases} \frac{2_{ml}K}{{}^{+}_{ml}h} & \mathbf{r}\in{}_{ml}\mathscr{T} \\ -\frac{1}{{}^{-}_{m}h} & \mathbf{r}\in{}_{m}\mathscr{W} \\ 0 & \text{elsewhere} \end{cases} \tag{13}$$

Expression (11) and (12), can be used for SPM and WGM if one assumes $L_m = 1$, or for attachment, with the pertinent L_m value, if:

$${}^{\pm}_{ml}\mathbf{W} = \begin{cases} {}^{\pm}_{m}\boldsymbol{\rho} & \text{for WGM} \\ \frac{{}_{m}l}{2}\,{}^{\pm}_{m}\boldsymbol{\rho} & \text{for SPM} \\ \begin{cases} {}_{ml}K\;{}_{ml}Q & \text{case } + \\ {}^{-}_{m}\boldsymbol{\rho} & \text{case } - \end{cases} & \text{for ATT} \end{cases} \tag{14}$$

being

$${}_{ml}Q = \frac{{}_{ml}l}{2}\,{}_{ml}\boldsymbol{\rho} - {}^{+}_{ml}h^2\left[\left(\tan\phi_b - \tan\phi_a\right)\hat{\mathbf{u}} + \frac{1}{2}\left(\frac{1}{\cos^2\phi_b} - \frac{1}{\cos^2\phi_a}\right)\hat{\mathbf{v}}\right] \tag{15}$$

and being the quantities herein defined as in [13, 15] and in Figure 4.

With a similar procedure, the term relative to the scalar potential can be written as:

$${}^{\pm}_{ml}M = \begin{cases} \pm 1 & \text{for WGM} \\ \pm{}_{m}l & \text{for SPM} \\ \begin{cases} -\frac{{}_{ml}\alpha}{{}_{m}t\alpha} & \text{case } + \\ 1 & \text{case } - \end{cases} & \text{for ATT} \end{cases} \tag{16}$$

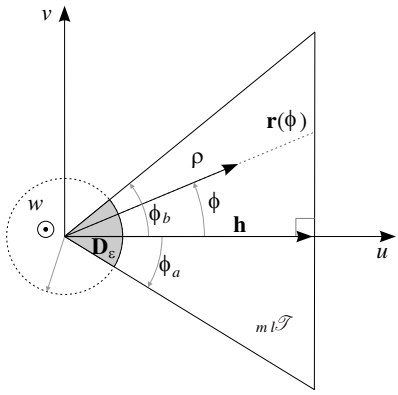

Figure 4. Local Cartesian coordinates system (u, v, w) and the local cylindrical coordinate system (ρ, ϕ, w).

To perform the calculation of current coefficients for the iterative solver, it is necessary to evaluate scalar and vector potential in all the central points of every elementary subdomain $\mathbf{a}^n({}^{\pm c}_{ml}\mathbf{r})$ and $\psi^n({}^{\pm c}_{ml}\mathbf{r})$. This can be done by substituting the geometrical and temporal discretization for the density current (5) in the expressions for the scalar and vector potentials, calculated at the nth time step and at point ${}^{\pm c}_{ml}\mathbf{r}$, obtaining:

$$\mathbf{a}^n\left({}^{\pm c}_{ml}\mathbf{r}\right) = \frac{\mu}{4\pi}\sum_{k=0}^{N-1}\sum_{h=0}^{n}\int_{\mathscr{D}_k^{\pm}}\frac{J_k^h T_h\left({}^{\pm}_{ml}\tau_k^n\right)\mathbf{f}_k\left(\mathbf{r}'\right)}{\left|{}^{\pm c}_{ml}\mathbf{r}-\mathbf{r}'\right|}\,d\mathbf{r}'$$

$$= \frac{\mu}{4\pi}\sum_{k=0}^{N-1}\sum_{h=0}^{n}J_k^h\left\{T_h\left({}^{\pm}_{ml}\tau_k^{n-}\right)\left[{}^{\pm}_{ml}\mathbf{K}_k^-\right]+\sum_{i=1}^{L_k}T_h\left({}^{\pm}_{ml}\tau_{ki}^{n+}\right)\left[{}^{\pm}_{ml}\mathbf{K}_{ki}^+\right]\right\} \quad (17)$$

being

$${}^{\pm}_{m}\mathbf{K}_k^{\pm} = \int_{\mathscr{D}_k^{\pm}}\frac{\mathbf{f}_k^{\pm}\left(\mathbf{r}'\right)}{\left|{}^{\pm c}_{m}\mathbf{r}-\mathbf{r}'\right|}d\mathbf{r}' \quad (18)$$

and being

$${}^{\pm}_{ml}\tau_{ki}^{n\pm} = t_n - \frac{\left|{}^{\pm c}_{ml}\mathbf{r}-\mathbf{r}_{ki}^{\pm}\right|}{c} \quad (19)$$

the time delay between the source point and the observation point.

It is important to note that the potentials are computed and stored only at discrete time instants t^n, but their value is needed at generic time instants according to the delay ${}^{\pm}_{ml}\tau_{ki}^{n\pm}$, from here stems the necessity of an interpolating time basis T_h.

The differential scalar potential it is:

$$\psi^n\left({}^{\pm c}_{ml}\mathbf{r}\right) = \frac{-1}{4\pi\varepsilon}\sum_{k=0}^{N-1}\sum_{h=0}^{n}\int_{\mathscr{D}_k^{\pm}}\frac{J_k^h T_h\left({}^{\pm}_{ml}\tau_k^n\right)\nabla'\cdot\mathbf{f}_k\left(\mathbf{r}'\right)}{\left|{}^{\pm c}_{ml}\mathbf{r}-\mathbf{r}'\right|}\,d\mathbf{r}'$$

$$= \frac{-1}{4\pi\varepsilon}\sum_{k=0}^{N-1}\sum_{h=0}^{n}J_k^h\left\{T_h\left({}^{\pm}_{ml}\tau_k^{n-}\right)\left[{}^{\pm}_{ml}S_k^{-}\right]+\sum_{i=1}^{L_k}T_h\left({}^{\pm}_{ml}\tau_{ki}^{n+}\right)\left[{}^{\pm}_{ml}S_{ki}^{+}\right]\right\} \quad (20)$$

being

$${}^{\pm}_{m}S_k^{\pm} = \int_{\mathscr{D}_k^{\pm}}\frac{\nabla'\cdot\mathbf{f}_k^{\pm}(\mathbf{r}')}{\left|{}_m\pm c\mathbf{r}-\mathbf{r}'\right|}\,d\mathbf{r}' \quad (21)$$

As it was for (11) and (12), also (17) and (20) are applicable to SPM and WGM if $L_k = 1$ and to an attachment if $L_k \geq 1$.

Computation of ${}^{\pm}_{m}\mathbf{K}_k^{\pm}$ and ${}^{\pm}_{m}S_k^{\pm}$ integrals may be performed analytically over wires, but must be performed numerically over triangles. This is an important point because an exact analytic solution is no source of additional numerical instability, whereas numerical integrals are approximated and can lead to an increased instability [10].

In both cases integrals are considered between geometrical primitives (wires and triangles) and not between single bases or weights [16]. Indeed every geometrical primitive may belong to the domain of several bases and test, hence computing the integral on the geometrical primitive allows for the evaluation of the basis/test integral as a summation of these latter, as shown in (17) and (20). This implies that the vector integral functions like (18) and (21) are decomposed into 2×2 scalar integrals for SPM-SPM, SPM-WGM, WGM-SPM and WGM-WGM evaluation, into $2\times(L_m+1)$ for SPM-ATT and WGM-ATT evaluation, $2\times(L_k+1)$ for ATT-SPM and ATT-WGM and into $(L_m+1)\times(L_k+1)$ for ATT-ATT evaluation.

Finally, substituting the potential expansion in (8), an implicit iterative operator is obtained as in [10]:

$$[\mathbf{Z}]\,J_k^n = \sum_{h=1}^{n}[\mathbf{F}]_h\,J_k^{n-h} + V_k^n \quad (22)$$

4. RADIATED FIELD

Once the transient currents on the scatter body have been determined, is possible to calculate the electric and magnetic fields anywhere and at any time outside the scatter [18, 19]. The scattered magnetic field $\mathbf{H}^s(\mathbf{r},t)$, at a point $\mathbf{r}$ is related to the vector potential, and hence

inducted currents by:

$$\mathbf{H}^s(\mathbf{r},t) = \frac{1}{\mu_0}\nabla \times \mathbf{a}(\mathbf{r},t) \tag{23}$$

From (2), and exploiting well known vector identities it is:

$$\mathbf{H}^s(\mathbf{r},t) = \int_S \left[\frac{\nabla \times \mathbf{j}\left(\mathbf{r}', t - \frac{R}{c}\right)}{4\pi R} - \frac{\hat{\mathbf{u}}_R}{4\pi R^2} \times \mathbf{j}\left(\mathbf{r}', t - \frac{R}{c}\right) \right] dS' \tag{24}$$

where $\hat{\mathbf{u}}_R$ is a unit vector directed as $\mathbf{r} - \mathbf{r}'$. If the far field is sought for, the second term in the integral (24) can be neglected.

By recalling that

$$\nabla \times \mathbf{j}\left(\mathbf{r}', t - \frac{R}{c}\right) = \frac{1}{c}\left.\frac{\partial \mathbf{j}(\mathbf{r}', t)}{\partial t}\right|_{t-\frac{R}{c}} \times \hat{\mathbf{u}}_R \tag{25}$$

and by indicating for brevity $t_R = t - \frac{R}{c}$, and its corresponding discretization with $t_R^n = t^n - \frac{R}{c}$, by using (5) for expanding the current densities, without any explicit differentiation between SPM, TWA and ATT, and by exchanging the summation and the integral the magnetic field can be written as:

$$\mathbf{H}^s(\mathbf{r},t^n) \approx \frac{1}{4\pi c}\sum_{k=0}^{N-1}\sum_{h=0}^{n}\int_{\mathscr{D}_k^{\pm}} J_k^h \left.\frac{\partial T_h(t)}{\partial t}\right|_{t_R^n} \cdot \frac{\mathbf{f}_k(\mathbf{r}') \times \hat{\mathbf{u}}_R}{R} dS' \tag{26}$$

The time instant t_R^n is related to the local position $\mathbf{r}'$ on the scatter body. Anyway, as it has already been done in the previous section, the spatial extension of each elementary sub domain is considered small compared to the shortest wavelength, hence we can assume the time variable t_R^n constant on the single subdomain and equal to the value relative to the central point of the subdomain itself. This way, the time first derivative is not related to the local vector $\mathbf{r}'$ any more and can be carried out of the integral.

In a far field approach, the distance R from the source to the observation point (Figure 5) can be approximated with the distance from the origin r, provided that the scatterer is close to the origin and the unit vectors $\hat{\mathbf{u}}_R$ and $\hat{\mathbf{u}}_r$ can be considered parallel. For the time delay, on the other hand the distance is better approximated by $R \approx r - \mathbf{r}' \cdot \hat{\mathbf{u}}_r$, and hence:

$$t^n_{R^{c\pm}_{ki}} = t^n - \frac{r}{c} + \frac{\mathbf{r}^{c\pm}_{ki} \cdot \hat{\mathbf{u}}_r}{c} \tag{27}$$

To efficiently evaluate and the far-scattered fields we need to define a time window in which the far field is non zero and restrict the

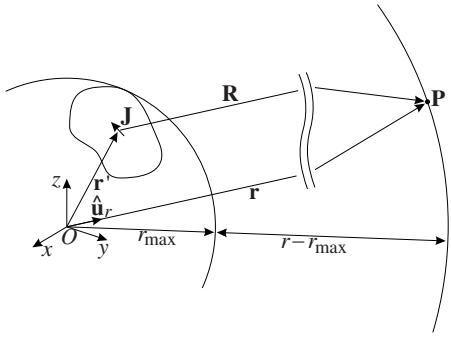

Figure 5. Far field time normalization problem.

computation to such window. Indeed in (26) the time summation in $h = 0, \ldots, n$ comprises several terms which are null *a priori* current samples which are relative to time instants h not far enough in the past cannot contribute to the field in the observation point at time t^n.

If $\bar{t}(\mathbf{r}')$ is the time at which a signal originated in $\mathbf{r}'$ at $t = 0$ arrives at the observation point, and $r_{\max}$ is the radius of the smallest sphere centered in the origin and containing the scattering object then, as a generic rule, no signal can reach the observation point before $\bar{t}(O) - r_{\max}/c$, being $\bar{t}(O) = r/c$.

With these considerations and defining $\bar{n} = \lfloor (\bar{t}(O) - r_{\max}/c)/\Delta t \rfloor$ (26) becomes

$$\mathbf{H}^s(\mathbf{r}, t^n) \approx \frac{1}{4\pi c} \sum_{k=0}^{N-1} \sum_{h=0}^{(n-\bar{n})} J_k^h \left\{ \sum_{i=1}^{L_k} \left[\left. \frac{\partial T_h(t)}{\partial t} \right|_{t^n_{R^{c+}_{ki}}} \cdot \frac{1}{r} \int_{\mathscr{D}^+_{ki}} \mathbf{f}_k^+(\mathbf{r}') dS' \right] + \left. \frac{\partial T_h(t)}{\partial t} \right|_{t^n_{R^{c-}_k}} \cdot \frac{1}{r} \int_{\mathscr{D}^-_k} \mathbf{f}_k^-(\mathbf{r}') dS' \right\} \times \hat{\mathbf{u}}_r \tag{28}$$

Basis function integrals in (28) are not dependent on the far field observation point direction or time instant, so they can be evaluated once for all and stored for later use. Whether they are linear, planar or attachment integrals, we can define:

$$\mathbf{F}^+_{ki} = \int_{\mathscr{D}^+_{ki}} \mathbf{f}_k^+(\mathbf{r}') \, dS' \qquad \mathbf{F}^-_k = \int_{\mathscr{D}^-_k} \mathbf{f}_k^-(\mathbf{r}') \, dS' \tag{29}$$

In evaluating the far-scattered field as a post-processing step, the time interpolating functions need to be derived. The analytic evaluation of time derivative of time base functions is not always

possible, or univocally determined as the time basis functions are peicewise continuous but can be non-differentiable on a finite discrete number of points [9, 10]. Only few interpolating time base functions that are continuous and with first derivative continuous are presented in literature as the exponential one [20] and the risen cosine defined in [7]. Anyway, the time derivative of time basis function can be analytically approximated at the discontinuity points, if the need arises, as a mean of the two left and right derivatives, which are guaranteed to exist as in [1]. The discontinuity in the time derivative is not a major issue since it actually appears in the scattered field only if the time delay between the observation point and the source is an integer number of Δt. This is statistically uncommon. Furthermore, since only a very reduced number of spatial basis of the whole domain can be at a delay which is an integer number of Δt, its effect is negligible with respect to the contribution of the whole body. By defining

$$\dot{T}_h(t) = \frac{\partial T_h(t)}{\partial t} \tag{30}$$

the following relation is obtained

$$r\mathbf{H}^s(\mathbf{r}, t^n) \approx \frac{1}{4\pi c} \sum_{k=0}^{N-1} \sum_{h=0}^{(n-\bar{n})} J_k^h \left\{ \sum_{i=1}^{L_k} \left[\dot{T}_h \left(t^n_{R^{c+}_{ki}} \right) \mathbf{F}^+_{ki} \right] + \dot{T}_h \left(t^n_{R^{c-}_k} \right) \mathbf{F}^-_k \right\} \times \hat{\mathbf{u}}_r \tag{31}$$

In (31), to obtain an evaluation of the scattered field independent from the distance r, the quantity $\mathbf{H}^s(\mathbf{r}, t^n)$ is normalized as $r\mathbf{H}^s(\mathbf{r}, t^n)$.

After the magnetic far-scattered field evaluation, the electric one can be recast as in (32), where ζ is the medium characteristic impedance.

$$\mathbf{E}^s(\mathbf{r}, t^n) = \zeta \mathbf{H}^s(\mathbf{r}, t^n) \times \hat{\mathbf{u}}_r \tag{32}$$

5. NUMERICAL RESULTS

The first test case analyzed is a scatter consisting of both wires and surface metal parts electrically connected. In particular, a 0.5 m long wire of radius $a = 5\,\text{mm}$ radius is connected to the center of a $0.5 \times 0.5\,\text{m}^2$ square horizontal plate. To show the advantages of the attachment modes also in time domain, the object is analyzed with different approaches: the first exploiting the attachment implementation presented here, and meshing the wire via WGM and the plate via SPM; the second exploiting only SPM, also for the wire part (Figure 6).

In the attachment case, the wire part is subdivided into 5 segments 0.1 m long each, while the surface part is subdivided into a regular mesh grid comprising 32 triangle patches, basis and test functions are piecewise linear for the WGM [9] and RWG for the SPM [5, 10], plus the attachment mode described in this paper.

In the SPM only case, the mesh structure composed by only planar parts common in literature for frequency domain analysis is used [18, 21, 22]. The wire is hence approximated as a strip and modeled by triangular patches and only RWG base/test functions are used. Modeling the wire part as SPM require a densest mesh, as it is evident in Figure 6.

The complete model of WGM-SPM-ATT (Figure 6(a)) requires 45 base/test functions (40 for the plate, 4 for the wires, 1 for the attachment), the SPM only (Figure 6(b)) requires for the same geometry 153 base/test functions. The second case solving system has hence more than three times the unknowns, and the equations, with respect to the first case. The use of a mixed mesh reduce the solving system dimensions, and hence reduce the computing resources and times. Furthermore, using the SPM model for the wire part introduces an asymmetry in the structure and results will present a dependency on the impinging plane wave direction, whereas, using the WGM model, the rotational symmetry of the wire is preserved.

The excitation used in the simulations is an unmodulated Gaussian pulse plane wave as in [10]:

$$\mathbf{e}^i(\mathbf{r},t) = \frac{A}{T\sqrt{\pi}}\mathbf{E}_0 e^{-\left[\frac{Bc}{T}\left(t-t_0-\frac{\mathbf{r}\cdot\hat{\mathbf{k}}}{c}\right)\right]^2} \tag{33}$$

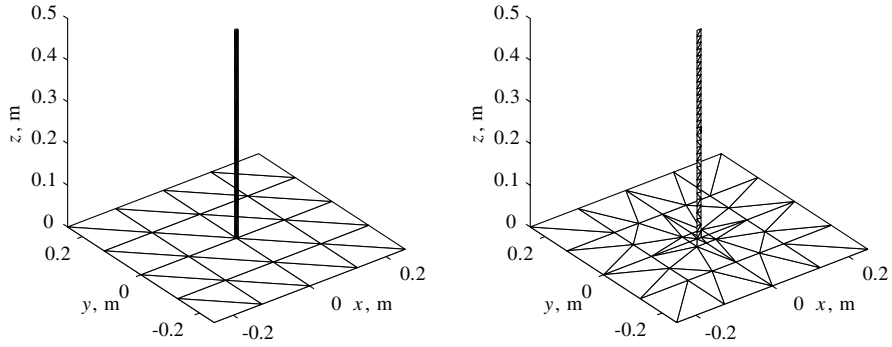

Figure 6. Wire and plate problem. (a) Presented model. (b) Makarov model [18].

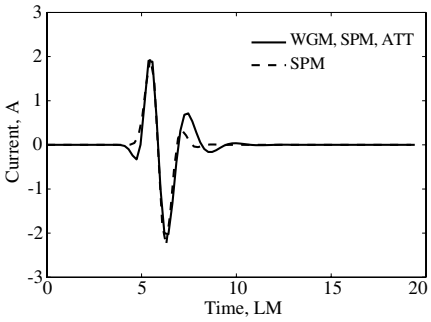

Figure 7. Time domain current in the wire geometry, 0.1 m above the planar part.

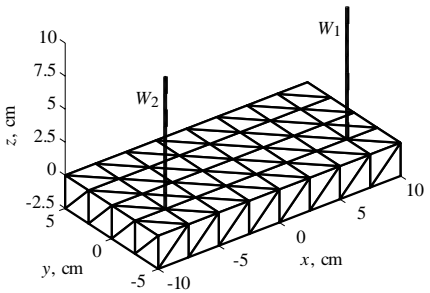

Figure 8. Geometry and mesh of the test set-up.

with: $\mathbf{E}_0 = 120\pi/\sqrt{2}\,(\hat{\mathbf{y}} - \hat{\mathbf{z}})\,\mathrm{V/m}$ the amplitude and direction of the incident electric field, $T = 2\,\mathrm{LM}$ the time length of the impulse expressed in light meters (LM) and $t_0 = 6\,\mathrm{LM}$ an appropriate delay of the pulse with respect to the starting time $t = 0$ of the simulation (used in (33) as the corresponding time expressed in seconds for units coherence). c is the speed of light and $A = 4\,\mathrm{LM}$ and $B = 4\,\mathrm{LMm}^{-1}$ are appropriate coefficients to maintain the correct physical dimensions. In the simulations the plane wave direction is $(\theta = 45°, \phi = 90°)$. The time basis is exponential as defined in [20] witch is a continuous function with a first time derivative continuous. The total simulated time span is 20 LM and the time discretization is $\Delta t = 0.7\,\mathrm{ns}$ (corresponds to about 0–700 MHz frequency range).

The time wave form for the current in the wire 0.1 m above the planar part is shown in Figure 7 for both models. Comparable results are obtained in both cases, even if memory and time requirements are much higher in the second case. Noticeable differences between the two models are due to the intrinsic anisotropy of the SPM-only approximation, where the wire, which is rotationally symmetric, is approximated via an infinitely thin strip. Furthermore, while the ATT model comprises, in this case, a wire and six triangular patches, the SPM-only model comprises just two patches on the plate and one in the strip modeling the wire [23], further worsening the anisotropic behavior since only y-directed currents on the plate (Figure 6(b)) do interact with the strip.

As a second example, a set up comprising a box $20 \times 10 \times 2.5\,\mathrm{cm}$ with two wires 10 cm long each, connected over the box is considered (Figure 8). The box itself is divided into a regular mesh grid comprising 112 triangles, while the two wires are divided into 8 segments each. Wire radius is 1.25 mm.

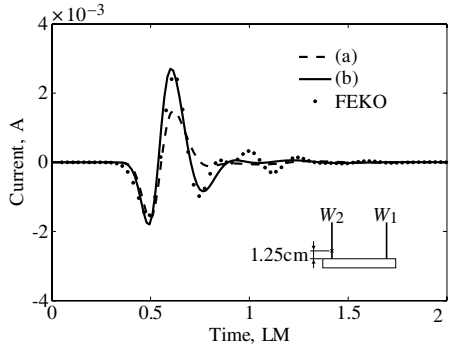

Figure 9. Time domain current in the first node to the second wire (W_2) and nearer to the box. (a) Without using the attachment model. (b) Considering the attachment model here presented. Symbols are relative to a simulation with commercial frequency domain MoM software (FEKO) on the connected structure (b).

Excitation is an unmodulated Gaussian pulse plane wave with: $\mathbf{E}_0 = 1\hat{\theta}\,\mathrm{V/m}$, $T = 0.25\,\mathrm{LM}$ and $t_0 = 0.5\,\mathrm{LM}$, the other parameters being the same as in the previous example. $\hat{\mathbf{k}} = -\left(\hat{\mathbf{x}} + \hat{\mathbf{y}} + \sqrt{2}\hat{\mathbf{z}}\right)/2$ is the unit vector of the plane wave propagation (corresponding to $\theta = 45°$, $\phi = 45°$ in a spherical reference). The time basis is exponential [20] hence continuous with continuous first time derivative. The total simulated time span is $2\,\mathrm{LM}$ ($6.667\,\mathrm{ns}$), and the time discretization is $\Delta t = 50\,\mathrm{ps}$.

Two cases are analyzed for the geometry: a) the wires have no electrical connection to the box, as in [10], where the attachment space basis/test function were not available; b) the wires are electrically connected to the box and the attachment space basis/test function described in the present paper are exploited. Both results are reported in Figure 9. As expected, introducing the attachment space basis function, the current flow between the box and the wire is evident as the current on the same wire node has a grater amplitude.

To validate the results, on the same graph the results obtained via a commercial MoM code in frequency domain (FEKO) on the structure with connected wires are superimposed. These results are obtained via inverse Fourier transform of frequency domain data. The noticeable difference between FEKO results and curve b), especially at the late time response, are entirely due to the spectrum discretization of the impinging Gaussian pulse, which is necessary to implement the series of frequency domain analyses and subsequent inverse Fourier transform, which cannot be done arbitrarily accurate without having to refine the

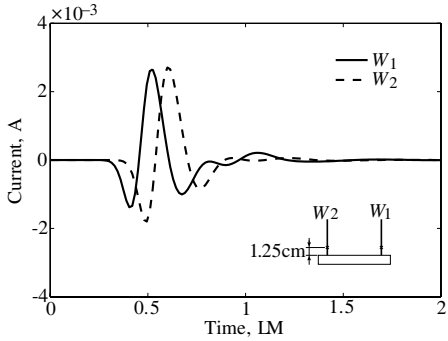

Figure 10. Time domain current in the first nodes nearer to the box for the first (W_1) and second wire (W_2).

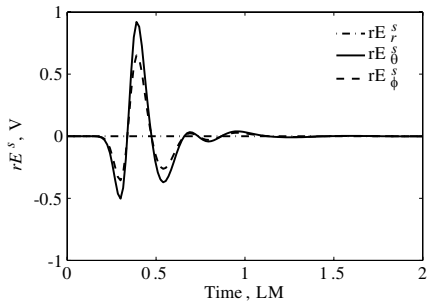

Figure 11. Normalized backscattered ($\theta = 45°, \phi = 45°$) far field components.

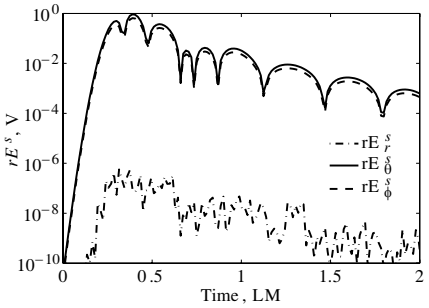

Figure 12. Normalized backscattered ($\theta = 45°, \phi = 45°$) far field components in semi-logarithmic scale.

spatial discretization, which would in turn rise computing time. Hence the difference in amplitude of late time oscillations.

To have a better understanding the induced current on the scatter body are sampled on both wires and reported in Figure 10. A time shift on the current on W_2 is evident as the incident field impinges first with W_1.

The mutual interaction between the two wires and the box causes a noticeable difference between the late time responses of the two wires. If these were two antennas, the knowledge of the signal distortion provided by the MoM-TD would be valuable. The backscattered ($\theta = 45°, \phi = 45°$) electric field is computed via (32) and (31). The electric field components, in spherical coordinates, are plotted in Figure 11. To better appreciate the amplitude of the backscattered

Table 2. Computing times.

	Test case 1 (Figure 6(a))	Test case 2 (Figure 6(b))	Test case 3 (Figure 8)
No. of basis/weight functions	45	135	172
No. of time steps	95	95	133
Computing time (seconds)	96	176	808

field, and the presence of cross-polarization components, the data are plotted also in semi-logarithmic scale in Figure 12. The time scale on the far-field plots is shifted as described in Section 4.

Finally Table 2 reports the computing times for the three examples, relative to a desktop PC with an Intel core 2 duo processor at 1.83 GHz with 2 GB of RAM. Anyway, by trying different solvers as in [24], differences in computation time and also in numerical stability can be obtained. A deep research for the best solver choice vs. computation time is needed, but this is outside the scope of this paper.

6. CONCLUSIONS

The wire-to-plate attachment problem in a time domain method of moment framework has been addressed. A set of bases/weights applied and their validity assessed. Some results over simple test cases illuminated by a wide band pulse shows the accuracy and effectiveness of the method. Results shows how a given structure can be more efficiently and accurately simulated if TWA and SPM are used together and with the proposed attachment model; the same structure discretized either with only TWA or only SPM gives less accurate results. Results are compared with a commercial code (FEKO) in frequency domain by performing several harmonic simulations and applying an IFT, while results match, the frequency domain + IFT procedure is much more lengthy and complex than the direct time domain analysis. The capability of the MoM-TD procedure of handling large bandwidth signals and transient is very valuable in antenna and microwave devices analysis and design.

REFERENCES

1. Rao, S. M., *Time Domain Electromagnetics*, Academic Press, 1999.

2. Zhang, G.-H., M. Xia, and X.-M. Jiang, "Transient analysis of wire structures using time domain integral equation method with exact matrix elements," *Progress In Electromagnetics Research*, Vol. 92, 281–298, 2009.
3. Harrington, R. F., *Field Computation by Moment Methods*, Macmillan Series in Electrical Science, MacMillan, New York, NY, 1968.
4. Martin, R. G., A. Salinas, and A. R. Bretones, "Time-domain integral equation methods for transient analysis," *IEEE Antennas Propag. Mag.*, Vol. 34, No. 3, 15–23, 1992.
5. Rao, S. M. and D. R. Wilton, "Transient scattering by conducting surfaces of arbitrary shape," *IEEE Trans. Antennas Propag.*, Vol. 39, No. 1, 56–61, 1991.
6. Bost, F., L. Nicolas, and G. Rojat, "A time-domain integral formulation for the scattering by thin wires," *IEEE Trans. Magn.*, Vol. 36, No. 4, 868–871, 2000.
7. Sadigh, A. and E. Arvas, "Treating the instabilities in marching-on-in-time method from a different perspective," *IEEE Trans. Antennas Propag.*, Vol. 41, No. 12, 1695–1702, 1993.
8. Guan, X., S. Wang, Y. Su, and J.-J. Mao, "A method to reduce the oscillations of the solution of time domain integral equation using laguerre polynomials," *PIERS Online*, Vol. 3, No. 6, 784–789, 2007.
9. Guarnieri, G., S. Selleri, G. Pelosi, C. Dedeban, and C. Pichot, "Innovative bases and weights for wire junctions in time domain moment method," *IET Proc. Microw. Antennas Propag.*, Vol. 153, 61–66, 2006.
10. Agastra, E., C. Dedeban, G. Guarnieri, S. Maddio, G. Pelosi, C. Pichot, and S. Selleri, "Space and time basis function design for the method of moments in time domain analysis of wire and planar structures," *Int. J. RF and Microw. Computer Aided Eng.*, Vol. 21, No. 5, 551–559, 2011.
11. Tekin, I. and E. H. Newman, "Method of moments solution for a wire attached to an arbitrary faceted surface," *IEEE Trans. Antennas Propag.*, Vol. 46, No. 4, 559–562, 1998.
12. Champagne, N. J., W. A. Johnson, and D. R. Wilton, "On attaching a wire to a triangulated surface," *Proc. IEEE Antennas and Propagation Society Int. Symp.*, Vol. 1, 54–57, 2002.
13. Yu, Y. and A. McCowen, "The fast-multipole method applied to open-PEC problems with triangular type wire-to-surface junctions," *COMPEL*, Vol. 27, No. 3, 682–702, 2008.

14. Taboada, J. M., J. L. Rodriguez, and F. Obelleiro, "Comparison of moment method solutions for wires attached to arbitrary surfaces," *Proc. IEEE Antennas and Propagation Society Int. Symp.*, Vol. 4, 2302–2305, 2000.
15. Taboada, J. M., J. L. Rodriguez, F. Obelleiro, and M. R. Pino, "Method of moments solution for wires attached to perfect electric conducting surfaces using floating attachment modes," *Proc. IEEE Antennas and Propagation Society Int. Symp.*, Vol. 4, 754–757, 2001.
16. Rao, S. M., D. R. Wilton, and A. W. Glisson, "Electromagnetics scattering by surfaces of arbitrary shape," *IEEE Trans. Antennas Propag.*, Vol. 30, No. 3, 409–418, 1982.
17. Hwu, S., D. R. Wilton, and S. M. Rao, "Electromagnetic scattering and radiation by arbitrary conducting wire/surface configurations," *Proc. IEEE Antennas and Propagation Society Int. Symp.*, Vol. 2, 890–893, 1988.
18. Makarov, S. N., *Antenna and EM Modeling with Matlab*, John Wiley & Sons, 2002.
19. Zhu, H., Z.-H. Wu, X. Y. Zhang, and B.-J. Hu, "Time-domain integral equation solver for radiation from dipole antenna loaded with general bi-isotropic objects," *Progress In Electromagnetics Research B*, Vol. 35, 349–367, 2011.
20. Hu, J.-L., C. H. Chan, and Y. Xu, "A new temporal basis function for the time-domain integral equation method," *IEEE Microw. Wireless Compon. Lett.*, Vol. 11, No. 11, 465–466, 2001.
21. Zhang, M., H.-C. Yin, and Z. Cao, "Transient scattering from arbitrarily shaped two-dimensional objects located on a rough surface," *PIERS Online*, Vol. 3, No. 5, 616–619, 2007.
22. He, S. and G. Zhu, "Analysis of transient scattering from 2-D rough surface using time domain integral equation method," *PIERS Online*, Vol. 1, No. 3, 313–317, 2005.
23. Wang, X., S.-X. Gong, J. Ling, and X.-M. Wang, "Interpolation scheme based on adaptive integral method for solving electrically large radiation problem by surface/surface configuration," *Progress In Electromagnetics Research M*, Vol. 11, 203–211, 2008.
24. Guan, X., S. Wang, Y. Su, and J.-J. Mao, "A comparison of performance of four methods in solving time domain integral equations for arbitrarily shaped conducting bodies," *PIERS Online*, Vol. 3, No. 2, 122–126, 2007.